# Diamagnetic chemical exchange saturation transfer (diaCEST) affords magnetic resonance imaging of extracellular matrix hydrogel implantation in a rat model of stroke.

Tao Jin, PhD, [1*], Francesca J. Nicholls, PhD, [1,2*], William R. Crum[5], D.Phil.,

Harmanvir Ghuman, B.Sc.[2,3], Stephen F. Badylak, DVM, PhD, M.D.[2,3,4],

Michel Modo, PhD.[1,2,3]

[1]Department of Radiology, [2]McGowan Institute for Regenerative Medicine,
[3]Department of Bioengineering, [4]Department of Surgery, University of Pittsburgh, Pittsburgh, PA
[5]Department of Neuroimaging, King's College London, London, UK

* Both authors contributed equally

***Corresponding Author:**
Dr. Mike Modo
University of Pittsburgh
McGowan Institute for Regenerative Medicine
3025 East Carson St
Pittsburgh, PA 15203
USA
+1 (412) 383 7200
e-mail: modomm@upmc.edu

**Abstract**

Chronic stroke results in significant brain tissue loss that causes permanent disability. Extracellular matrix (ECM) is widely used as an inductive biological scaffold to repair soft tissue after injury by promoting the formation of functional site appropriate remodeling of the injected material. However, there is a general lack of non-invasive imaging methods to monitor the distribution of ECM after injection and its biodegradation over time. Herein, we describe the use of diamagnetic chemical exchange saturation transfer (CEST) magnetic resonance imaging to monitor the distribution of an ECM hydrogel after intracerebral implantation into a stroke cavity. In vitro imaging indicated a robust concentration-dependent detection of the ECM precursor and hydrogel at 1.8 and 3.6 ppm, which broadly corresponded to chondroitin sulfate and fibronectin. This detection was robust to changes in pH (5.0-7.0) and improved at 37 °C. In vivo implantation of an ECM hydrogel into the stroke cavity in a rat model corresponded macroscopically to the distribution of biomaterial as indicated by histology, but mismatches were also evident. Indeed, CEST imaging also detected an endogenous upregulation of ECM molecules in the infarct environment. To account for this endogenous activity, pre-implantation images were subtracted from post-implantation images to yield a selective visualization of ECM hydrogel distribution in the stroke cavity and its evolution over 7 days. However, the CEST detection of ECM returned to baseline within 3 days. A selective acute imaging of ECM hydrogel distribution within the stroke cavity is hence feasible, but further development is required to warrant a specific and selective long-term monitoring.

**Keywords:** MRI, Extracellular Matrix, Hydrogel, Tissue Engineering, Stroke, Brain, Regenerative Medicine, Chemical Exchange Saturation Transfer, Chondroitin Sulfate, Fibronectin

## Graphical Abstract

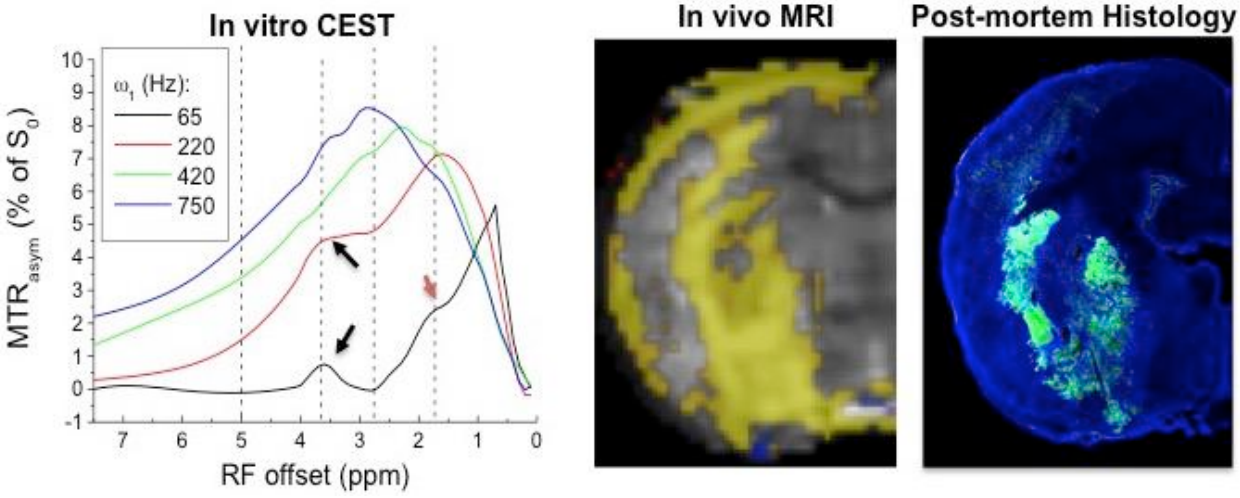

## 1. Introduction

The extracellular matrix (ECM) constitutes 20% of brain volume [1]. Stroke related infarcts result in the loss of neurons and other cells, but the extracellular matrix is gradually cleared to create an extracellular fluid (ECF)-filled tissue cavity [2]. Although neural stem cell transplantation in the peri-infarct tissue can alleviate some behavioral deficits, it does not replace lost tissue [3]. Instead, a structural support is required for cells within the cavity to develop a *de novo* tissue [4, 5]. Transplantation of neural stem cells in a hydrogel produced from extracellular matrix can efficiently repopulate the tissue cavity [6]. ECM hydrogels and sheets are extensively used for regenerative medicine in clinical settings to repair tissue defects, ranging from bladder reconstruction, muscle regeneration to breast reconstruction [7].

ECM can be formulated to reside in a liquid phase at room temperature and gel at brain temperature. These gelation properties are dependent on the collagen concentration within the preparation. Indeed, ECM hydrogels at different concentrations show retention within the cavity >3 mg/mL, whereas lower concentrations show poor gelation and permeate into the peri-infarct tissue [8]. Gelation is hence a key factor in providing a structural support within the cavity. Injection and hence retention of the ECM at an appropriate concentration inside a brain cavity is challenging, because a minimally invasive approach is required to avoid damage to brain tissue and the skull creates a closed environment [9]. The use of injection-drainage, where the appropriate concentration of ECM material is delivered at the given concentration, while ECF is drained, can achieve complete

coverage of the lesion cavity [8]. However, non-invasive imaging, such as magnetic resonance imaging (MRI), is required to define the cavity volume, as well as the injection-drainage access points.

Injection of ECM into the fluid-filled stroke cavity changes the diffusion characteristics of this environment and hence provides an indirect means to visualize changes in this environment [6, 10]. Indeed, $T_2$- and diffusion-weighted MRI have been suggested for the monitoring of tissue development from an acellular matrix [11, 12]. However, these measurements do not actually detect the material itself, nor do they afford a monitoring of the biomaterials' degradation. In some cases, the biomaterial has a very distinctive MR signature that can be used to contrast the implant versus host tissue [13, 14]. However, most scaffolding material is designed to biodegrade as host cells invade the material and gradually replace it, hence becoming indistinguishable from host tissue. In these cases, MR contrast agents can be integrated into, for instance, hyaluronic acid (HA)-based hydrogels, to afford a specific visualization of their location and degradation [15, 16].

Contrast agents only serve as a surrogate and do not directly visualize the injected material; similar degradation profiles are essential for these to report adequately on the presence of scaffolding material. Incorporation of contrast agents into the scaffold will further require additional safety scrutiny from regulators [17, 18]. Ideally, an imaging method therefore will not require the addition of MR contrast agents and will directly detect the injected material and its degradation profile. As ECM molecules are known to have MR-detectable

effects on water molecules that can be detected using chemical exchange saturation transfer methods (CEST) [19, 20], this principle can be exploited to directly detect the scaffold material. For instance, addition of gelatin to HA hydrogels can be used to detect the HA implant using diamagnetic CEST (diaCEST) [21]. Preferably no additional molecules are required to afford detection. Hydrogels derived from ECM that is manufactured by decellularization of a source tissue retain most molecules and hence potentially provide a multitude of molecules that can exert CEST effects. We here described the in vitro characterization of CEST effects induced by ECM in its liquid form and upon gelation, as well as their in vivo detection in a rat model of stroke with histological validation.

## 2. Methods

### 2.1. Extracellular matrix hydrogel

ECM was derived from the basement membrane and tunica propria of porcine urinary bladder (Tissue Source, Lafayette, IN). A mechanical delamination of the luminal epithelium and subjacent layers was followed by decellularization. Decellularization of the tissue was accomplished by 0.1% peracetic acid in 4% ethanol (v/v; 120 min; 300 rpm) and agitation prior to washing out of cellular components with PBS and deionized water rinses. Confirmation of decellularization was achieved using a series of measures (Hematoxylin & Eosin, 4',6-diamidino-2-phenylindole (DAPI) staining, agarose gel electrophoresis, and

measurement of DNA content). This material was lyophilized, comminuted, and solubilized with pepsin (1 mg/mL) in 0.01 N HCl prior to neutralization with 0.1 N NaOH. The final product was an injectable liquid at room temperature (21 °C) that formed a hydrogel at concentration >3 mg/mL at brain temperature (37 °C) [8]. Concentrations of 0 (PBS only), 2, 4, 6, and 8 mg/mL were used for *in vitro* experiments, whereas only 8 mg/mL was used for *in vivo* experiments. Matristem™ (ACell Inc. Columbia, MD) was used for comparison of a commercially available UBM-ECM product.

### 2.2. In vitro CEST imaging

*Hardware:* MR Images were acquired on a 9.4 T horizontal bore system interfaced to a DirectDrive 2 console (Agilent, Santa Clara, CA, USA). For phantom studies, a volume coil with an internal diameter of 38 mm was used (Agilent, Santa Clara, CA, USA). For *in vivo* studies, a custom made volumetric birdcage quadrature coil (Virtumed LLC) achieving a radiofrequency (RF) power input of up to 55 μT / 5 s with an internal diameter of 36 mm and effective length of 25 mm was used.

*CEST imaging*: All *in vitro* imaging was carried out at room temperature (apart from the varied-temperature experiments). Two sets of imaging parameters were adopted. CEST images were acquired by 2-shot spin-echo echo planar imaging (EPI) with FOV = 50 mm x 25 mm, matrix 128 x 64, TR = 10 s, and TE = 7.4 ms. A $B_1$ map was first acquired to calibrate the transmit power for the CEST studies and evaluate the $B_0$ homogeneity. Because the spatial variation of $B_1$ is <15% for

all of our phantoms, no correction of the $B_1$ inhomogeneity was applied. The CEST sequence was used to acquire Z-spectra between -8 to +8 with 43 interval offsets. The interval was chosen to be uneven since the chemical shift of most endogenous labile protons from water was less than 4 ppm. Thus the interval was 0.2 ppm from -1 to 1 ppm, 0.25 ppm from 1 ppm to 4 ppm and -1 ppm to -4 ppm, and 1 ppm from 4 to 8 ppm and -4 to -8 ppm. Additionally, images were acquired at offsets of 300 ppm for normalization. A $B_0$ map was obtained by using the water saturation shift referencing (WASSR) scheme [22], where a low power saturation (10 Hz) pulse was applied for 1 s, with 31 offset values ranging from -0.3 to 0.3 ppm in 0.02 ppm steps. In data sets where a significant $B_0$ inhomogeneity ($B_0$ variation >10Hz) was detected, the RF offset of images were interpolated to a 1 Hz interval on a pixel-by-pixel basis and shifted according to the $B_0$ map. Optimization of the saturation power was explored using an array (65, 220, 420, 750 Hz) of saturation frequencies. For saturation power of ≤420 Hz, the saturation duration was 5 s. For the highest power of 750 Hz, the direct water saturation (DWS) became significant even at 2-3 ppm. To minimize DWS and RF heating, an off-resonance spin-lock sequence was used [23, 24], and the irradiation duration was reduced to 3 seconds. Data were processed in MATLAB to generate magnetization transfer ratio asymmetries ($MTR_{asym}$), which were calculated from [25]

$$MTR_{asym}(\Omega) = [S_{sat}(-\Omega) - S_{sat}(\Omega)] / S_{sat}(300\,ppm),$$

where $S_{sat}(\Omega)$ is the signal intensity with a saturation pulse at frequency offset of $\Omega$. All subsequent experiments used an acquisition frequency of 220 Hz.

### 2.3. Temperature and pH effects on CEST signal

Chemical exchange is highly sensitive to temperature and pH. To probe the effects of temperature and pH on the CEST signal, both variables were arrayed and CEST images were acquired. For this, 8 mg/mL ECM hydrogel samples were created where pH was neutralized (pH 7). To adjust pH, Sodium hydroxide or Hydrochloric acid were added to the hydrogels and pH was confirmed with a pH spear (Eutech Instruments). ECM samples with an array of pH (5.5, 6.0, 6.5, 7.0) in 2 mL Eppendorfs were placed in 4% Agar holders. A temperature probe was placed into the Agar. These samples were placed into the MR scanner and temperature was controlled by circulating hot air to reach room temperature (21 °C), body temperature (37 °C) and an intermediate transition temperature (30 °C).

### 2.4. Liquid phase versus hydrogel ECM

In order to assess whether the gelation state of the ECM affects its detection, both liquid and gelled samples were imaged. 8 mg/mL ECM was prepared, and incubated for 40 min at 37 °C to allow gelation. Meanwhile, fresh ECM was prepared (with no gelation step) and maintained on ice until imaging. Samples were imaged at 21 °C.

### 2.5. Preparation of individual ECM components

To ascertain which ECM components are contributing to the CEST signal, purified proteins (Table 1) and artificial cerebro-spinal fluid (aCSF, Harvard Apparatus, 597316) were imaged separately for comparison with the ECM-derived signal. Solutions were made up in PBS and samples were imaged at 21 ºC.

### 2.6. Middle cerebral artery occlusion – a rat model of stroke

All animal procedures complied with the US Animals Welfare Act (2010) and were approved by the University of Pittsburgh Institutional Animal Care and Use Committee (IACUC). As previously described, 14 male Sprague-Dawley rats (260±15 g, Taconic Labs, USA) underwent transient intraluminal right middle cerebral artery (MCA) occlusion, a rat model of stroke [26]. For this, under isoflurane (4% induction, 1% maintenance in 30% $O_2$) anesthesia, a 5-0 silicon rubber-coated monofilament (503556PK10, Doccol, USA) was advanced to the ostium of the MCA in the circle of Willis and the MCA was occluded for 70 minutes prior to reperfusion. After recovery from anesthesia, animals were assessed for forelimb flexion and contralateral circling with daily post-operative care and neurological assessment until they recovered pre-operative weight [26, 27].

### 2.7. In vivo CEST imaging

Rats were anesthetized with isoflurane (4% induction, 1% maintenance). $T_2$-weighted images were acquired using a Fast Spin Echo Multi Slice sequence to

determine the location of lesion and to select the slices for CEST imaging (TR = 8 s, TE = 53 ms, number of segments = 16, number of averages = 4, 30 x 30 mm FOV, 128 x 128 matrix, 42 slices with 0.5 mm slice thickness). Tissue volume loss was based on a hyperintense signal on $T_2$-weighted images that were thresholded at 1 standard deviation above the mean of a rectangular region of interest (ROI) in the contralateral hemisphere, encompassing striatum, corpus callosum and neocortex [28]. Rats with lesion volume <40 $mm^3$ (i.e. 40 µl) were excluded [8]. $T_2$-weighted images also served as anatomical reference for CEST image overlays. For a proof-of-principle of detection, 3 MCAO rats with ECM hydrogel injection (see below) underwent CEST imaging 24 hours after implantation. To evaluate the time-dependence of the CEST effect, 3 groups of rats (MCAo only, n=3; MCAo+PBS, n=3; MCAo+ECM hydrogel, n=4) were imaged 4 times; namely, pre-injection, 1, 3 and 7 days after the post-injection.

For CEST imaging, $B_1$ and $B_0$ maps were first obtained, similar to phantom studies. To acquire the Z-spectrum, a saturation pulse with a power of 220 Hz and a duration of 2 s was applied. Images were acquired immediately after the saturation with a 2-shot spin-echo EPI. 43 different RF offsets were acquired from -8 to +8 ppm, as for the phantom studies. The parameters for imaging were: TR = 6.5 s; TE = 7.6 ms; FOV = 30 x 30 mm; matrix size = 96 x 96; 5 slices with 1 mm thickness. CEST images were thresholded to 3 standard deviations of the contralateral hemisphere to visualize only signal that is above the noise threshold and the baseline CEST signal (Supplementary Figure 1).

*Image Registration*: The baseline MR scan of a single case was chosen as a reference and all structural MR images were rigidly (i.e. with 6 degrees of freedom) registered to this reference using a previously described registration method [29] based on the FLIRT software [30]. For each rat at each time-point, a composite transformation was obtained by combining the transformation of each diaCEST image onto the corresponding MR image (derived from scanner positional information) with the transformation of the MR image onto the reference scan. Thus, all structural MR scans and all diaCEST images were rigidly registered into the same reference space. For accurate serial analysis, the post-treatment MR scan of each rat was further registered directly to the pre-treatment scan and the same transformation was applied to the associated diaCEST images.

*Post-Processing*: Mean structural and diaCEST images were computed for each group (MCAO only, PBS and ECM) in the reference space. Change in diaCEST signal in each rat over time was obtained by subtracting the pre-treatment image from the corresponding post-treatment images. To establish a suitable physiological noise level in the CEST images, a region of interest was drawn spanning the contra-lateral hemisphere in the reference MR image. This region was used to obtain the mean and standard deviation signal in each registered diaCEST image and in each diaCEST serial subtraction image. A threshold range of mean ± 3 std. dev. was used to exclude all signal within the range typically seen in the contra-lateral hemisphere (Supplementary Figure 2).

### 2.8. Implantation of ECM hydrogel

Fourteen days post-MCAo, rats underwent the implantation procedure by placement into a stereotactic frame (Kopf, USA) under isoflurane anesthesia (1.5% in 30% $O_2$) prior to drilling of burr holes at the appropriate coordinates for injection and drainage using a frame-mounted drill [8]. The injection volume of biomaterial was equivalent to the lesion volume, as determined by the hyperintense volume range on MR images (40-180 µL). The ECM was taken-up into a 250 µl Hamilton syringe with a 24 G beveled tip metal needle (Hamilton) mounted on the frame. The syringe/needle was advanced to the appropriate coordinates for biomaterial injection, whereas a 24 G cannula was placed in position to drain ECF. Injection of ECM hydrogel (8 mg/mL) was controlled using a frame mounted injection pump (World Precision Instruments, USA) at a constant speed of 10 µL/min. After the injection was complete, the needle and cannula were left in place for 5 minutes before being slowly removed from the brain with burr holes being filled with bone wax (Fisher) prior to suturing. LX4 (Ferndale, containing 4% Lidocaine) was topically applied as an analgesic, and Buprenex (0.05 mg/kg) was administered sub-cutaneously.

### 2.9. Immunohistochemistry

To analyze the distribution of the ECM hydrogel within the lesion cavity, rats were transcardially perfused with 0.9% saline followed by 4% paraformaldehyde (in 0.2 M PBS) 1 or 7 days post-implantation to fix brain tissue prior to its removal from the skull. Brains were post-fixed in 4% paraformaldehyde for 24 h prior to being

cryopreserved in 30% sucrose with sodium azide (Sigma) at 4° C. Histological sections (50 µm thickness) were cut on a cryostat (Leica) directly onto microscopic slides. Brain sections were washed 3 x 5 minutes with 0.01 M PBS, followed by one hour in blocking solution (PBS + 0.05% Triton X-100 + 10% Normal Goat Serum, NGS, Vector). Primary antibodies were then applied, consisting of rabbit anti-collagen I (1:250, Abcam, AB34710), mouse anti-fibronectin (1:150, Abcam, AB6328), mouse anti-chondroitin sulfate (1:200, Abcam, AB11570) and a chicken anti-Glial Fibrillary Acid Protein (GFAP, 1:3000, Abcam, AB4674) antibody diluted in blocking solution (0.05% Triton X-100, 10% NGS in PBS). Sections were incubated at 4 °C overnight. After rinsing of the primary antibodies (3x10 min PBS), appropriate secondary Alexa Fluor 488 and 555 antibodies (Life Technologies) were applied for 1 hour. Secondary antibodies were washed off and sections were incubated with Hoechst (1 µg/mL, Sigma, 14533) for 10-15 min prior to 3 x 5 min washes in PBS and being coverslipped with Vectashield for fluorescence (Vector Laboratories). Visualization of antibodies was performed on a fluorescence microscope (M2 Axioimager, Zeiss) with a monochrome camera driven by Stereo Investigator image capture software (MBF Bioscience).

## 3. Results

### 3.1. In vitro CEST characteristics of extracellular matrix hydrogel

Extracellular matrix (ECM) contains a variety of molecules that can potentially affect chemical exchange saturation transfer (CEST) with water. To define an acquisition paradigm that will afford a robust detection, an array of frequencies was applied to record the chemical exchange saturation transfer ($S_{Sat}/S_0$) of ECM hydrogel (8 mg/mL) over a relevant range of radiofrequency (RF) offsets (Figure 1A). Blips in the spectra are evident indicating specific exchange sites, especially around +3.6 ppm (65 Hz), but also a broader underlying asymmetry between the negative and positive offset at higher frequencies. Indeed, magnetization transfer asymmetry ($MTR_{asym}$), which was obtained by subtracting the positive from the negative offset, reveals effect sizes of up to 8.5% at 2.8 ppm with 750 Hz (Figure 1B). Indeed, the most significant asymmetry was apparent with a frequency of 750 Hz. However, the smoothness of the curve did not clearly reveal a specific exchange site. In contrast, the lower frequencies of 220 Hz and 65 Hz reveal specific exchange sites at 3.6 ppm, 2.8 ppm, as well as at 1.8 ppm. The 65 Hz frequency provides the sharpest definition of these sites, but the effect size is markedly reduced compared to the 4.3% (3.6 ppm) and 6.5% (1.8 ppm) $MTR_{asym}$ at 220 Hz. A 220 Hz acquisition hence provides specific exchange site, as well as marked contrast for the ECM hydrogel. Images of the $MTR_{asym}$ further indicate a robust visualization of the ECM hydrogel using 220 Hz compared to 65 Hz (Figure 1C). Although 420 Hz and 750 Hz also afforded a robust detection with a more significant asymmetry at all sampled frequencies, these effects are less specific, which renders them more susceptible to unspecific MTR effects that

could compromise a specific detection of ECM hydrogels in vivo. All subsequent experiments therefore used the 220 Hz frequency for acquisition.

### 3.2. Magnitude of ECM CEST signal is affected by temperature

As the CEST signal is affected by both temperature and pH (due to changes in the chemical exchange rate), both were arrayed to establish their effect on detection of the ECM hydrogel (8 mg/mL). Indeed, the temperature of the ECM will increase from room temperature (21 °C) to body temperature (37 °C) upon implantation and allow gelation of the material. Although pH of the ECM hydrogel is neutral upon injection, the infarcted area has a low pH and could reduce pH in the injected ECM. There was an overall effect of temperature, which increased $MTR_{asym}$ at 1.8 ppm by ~42%, from 7.3% at 21 °C to 10.4% at 37 °C (pH 7.0) (Figure 2A). Since CEST signal is nearly proportional to the water $T_1$, this increase is likely caused by an increase of $T_1$, which increased from 2.8 s at room temperature to about 4.0 s at 37 °C. The same pattern was observed for all pH values, but notable differences in the z spectra were also apparent. For instance, at 21 °C, the $MTR_{asym}$ at 2.8 ppm was much more pronounced for low pH values, but this difference gradually eroded with an increase in temperature. Furthermore at 37 °C, pH 7 was increased from the other pH values at 1.8 ppm, but only by ~16%. Temperature therefore increased the $MTR_{asym}$ overall, which is advantageous for detection in the brain, whereas the effect of pH was negligible.

### 3.3. ECM concentration affects magnitude of CEST signal

AS ECM is injected into the brain at 21 °C, it transitions from a liquid phase to a hydrogel state at 37 °C by cross-linking of proteins, such as collagen I. The cross-linking and the associated rheological changes are also dependent on the concentration of the ECM. The physical characteristics of the ECM therefore change in a concentration-dependent fashion and could affect detection using diaCEST. In the liquid phase, a robust detection of the ECM is observed at 8 mg/mL with a dose-dependent decrease in signal down to 2 mg/mL (Figure 2B). A 0 mg/mL (PBS only) condition did not produce any detectable $MTR_{asym}$. Formation of a hydrogel (i.e. bringing the ECM to 37 °C) also produced a dose-dependent signal (Figure 2C). However, separation between 2 and 4 mg/mL was less clear, potentially due to a lack of gelation of 2 mg/mL. The 4 mg/mL hydrogel condition hence produces an $MTR_{asym}$ that is akin to the 2mg/mL liquid $MTR_{asym}$. It is noteworthy that these $MTR_{asym}$ properties of ECM hydrogel are also evident in the commercially available ECM product Matristem (Supplementary Figure 3). A potential confound of the dose-dependent ECM $MTR_{asym}$ is pepsin, which is also added during the ECM preparation in a dose-dependent fashion. However, different doses of pepsin did not produce an $MTR_{asym}$ that could confound the ECM detection (Figure 2D).

### 3.4. Chondroitin sulfate and fibronectin are prominent components of ECM hydrogel CEST signal

As the ECM hydrogel is an agglomeration of different molecules present in tissue, it is unclear what specific molecules contribute to the $MTR_{asym}$. Individual

components were hence prepared to evaluate their $MTR_{asym}$ for comparison with the ECM-induced $MTR_{asym}$. Some ECM molecules (collagen I, heparin sulfate) produced negligible (<1%) $MTR_{asym}$, whereas others (collagen IV, hyaluronic acid, laminin, vitronectin) induced minor effects of 1-2.5% (Figure 3A). In contrast, chondroitin sulfate and fibronectin produced significant $MTR_{asym}$ of 4-7% at 1.8 ppm. It is intriguing to observe that these two molecules produce an overlapping $MTR_{asym}$ very similar to ECM, with a combination of both replicating the overall shape of an ECM hydrogel-induced $MTR_{asym}$ (Figure 3B).

As the application of ECM hydrogel will require injection into the fluid-filled cavity caused by a stroke, another factor potentially affecting the specificity of detection is the presence of extracellular or cerebrospinal fluid (CSF). Artificial CSF produced a 3.5% $MTR_{asym}$ at 1 ppm and 1.7% at 1.8 ppm (Figure 3A), which is very similar to that observed from HA, but distinct from ECM. ECM hydrogel can therefore be specifically detected in contrast to potentially confounding variables (PBS, Pepsin, CSF) and produce a robust dose-dependent $MTR_{asym}$.

### 3.5. In vivo detection of ECM hydrogel distribution in a rat model of stroke

Upon ECM hydrogel implantation into the cavity 14 days post-stroke, a CEST signal covering the lesion was evident 24 hours post-injection in all animals (Figure 4A). The CEST signal highlighted the anterior-posterior distribution of ECM and its macroscopic comparison to histology further confirmed that the signal corresponded to the area filled with ECM hydrogel (Figure 4B). However, a more detailed comparison between the CEST and histology image revealed

subtle differences that indicate that some of the CEST signal is not specific to the injected material (Figure 4C). Specifically, damaged peri-infarct tissue, as well as areas with a T2 hyperintense signal, also overlap with the CEST signal, but do not contain ECM hydrogel as revealed by collagen I staining, hence suggesting that some endogenous molecules might be upregulated in these areas and account for these areas of discrepancy. Nevertheless, the overall distribution of the ECM hydrogel and CEST signal is comparable and reveals, for instance, material that unexpectedly leaked into the lateral ventral (Figure 4D).

### 3.6. In vivo specificity and evolution of ECM hydrogel CEST signal

The presence of a baseline CEST signal, as well as its increase in damaged tissue, question the specificity of the approach for ECM hydrogel. Indeed, in the contralateral undamaged hemisphere, a weak <5% CEST signal at 1.8 ppm can be found (Figure 5). This CEST signal is mainly from the intracellular proteins and metabolites, but the intensity is relatively low due to the short tissue $T_2$ (~40 ms at 9.4 T) and the large direct water saturation effect. A slightly larger signal of up to 5% is also present within the lateral ventricles, whereas the signal within the lesion cavity is significantly increased compared to undamaged brain and ventricles to 8.6% $MTR_{asym}$. Note the larger CEST signal in the lesion cavity does not necessarily indicate a higher protein/ECM concentration. Besides the chemical exchange mediated relaxation, the CEST signal is also affected by other relaxation effects, such as $T_1$, $T_2$ and direct water saturation. These relaxation effects are expected to be smaller in the lesion cavity due to its higher

water content. Nevertheless, implantation of ECM hydrogel within this same area dramatically increased the signal to >20% $MTR_{asym}$. It is hence plausible that endogenous ECM molecules produced a weak signal in the lesion cavity, but that the injection of ECM hydrogel dramatically increased this signal to a level that is very distinct in its magnitude from the endogenous $MTR_{asym}$..

To selectively visualize the distribution of the ECM hydrogel, it is therefore necessary to account for this endogenous signal. This can be achieved by acquiring a pre-implantation baseline image that is subtracted from post-implantation images. Using this post-processing of the CEST images, the distribution of ECM hydrogel can be specifically and selectively visualized at different time points (Figure 6). Consistently the injection of ECM hydrogel in 4 animals lead to an increased signal in the lesion cavity by 1 day post-implant. In two animals with a large well-defined $T_2$-weighted hyperintense lesion cavity, a very robust and cohesive signal increase can be observed with >20% $MTR_{asym}$. In one animal (rat 3), a more irregular lesion cavity also showed a clear increase in $MTR_{asym}$ in the cavity, but patches adjacent to the main area were evident. In rat 4, the detection of the ECM hydrogel was less robust. In all animals, the signal due to the ECM hydrogel dramatically reduced within 3 days post-implantation to reach baseline levels and below baseline by day 7. These observations were also supported by $MTR_{asym}$ plots of the lesion cavity at each time point. Nevertheless, histology at day 7 revealed a robust presence of ECM hydrogel in the lesion cavity in all animals.

### 3.7. Group comparison of CEST signal with control conditions

To afford a group comparison of the CEST signal due to the ECM hydrogel injection, animals were coregistered and mean images were created for a MCAo only, a vehicle (PBS) injection, as well as an ECM injection condition (Figure 7). In the MCAO only condition, no change of the CEST signal in the stroke area was evident over 7 days. A vehicle injection revealed a slight increase in the CEST signal in damaged tissue 1 day post-injection, but upon further inspection this was only evident in 1 animal out of 4. This CEST signal is mainly from the intracellular proteins and metabolites, but the intensity is relatively low due to the short tissue $T_2$ (~40 ms at 9.4 T) and the large direct water saturation effect. A slightly larger signal of up to 5% is also present within the lateral ventricles, whereas the signal within the lesion cavity is significantly increased compared to undamaged brain and ventricles to 8.6% $MTR_{asym}$. Note the larger CEST signal in the lesion cavity does not necessarily indicate a higher protein/ECM concentration. Besides the chemical exchange mediated relaxation, CEST signal is also affected by other relaxation effects such as $T_1$, $T_2$ and direct water saturation, and these relaxation effects are expected to be smaller in lesion cavity due to its higher water content. Nevertheless, implantation of ECM hydrogel within this same area dramatically increased the signal to >20% $MTR_{asym}$. It is hence plausible that endogenous ECM molecules produced a weak signal in the lesion cavity, but that the injection of ECM hydrogel dramatically increased this signal to a level that is very distinct in its magnitude from the endogenous $MTR_{asym}$.

To selectively visualize the distribution of the ECM hydrogel, it is therefore necessary to account for this endogenous signal. This can be achieved by acquiring a pre-implantation baseline image that is subtracted from post-implantation images. Using this post-processing of the CEST images, the distribution of ECM hydrogel can be specifically and selectively visualized at different time points (Figure 6). Consistently the injection of ECM hydrogel in 4 animals lead to an increased signal in the lesion cavity by 1 day post-implant. In two animals with a large well-defined $T_2$-weighted hyperintense lesion cavity, a very robust and cohesive signal increase can be observed with >20% $MTR_{asym}$. In one animal (rat 3), a more irregular lesion cavity also showed a clear increase in $MTR_{asym}$ in the cavity, but patches adjacent to the main area were evident. In rat 4, the detection of the ECM hydrogel was less robust. In all animals, the signal due to the ECM hydrogel dramatically reduced within 3 days to reach baseline levels, and dropped to a level below the baseline at day 7. These observations were also supported by $MTR_{asym}$ plots of the lesion cavity at each time point. Nevertheless, histology at day 7 revealed a robust presence of ECM hydrogel in the lesion cavity in all animals.

### 3.7. Group comparison of CEST signal with control conditions

To afford a group comparison of the CEST signal due to the ECM hydrogel injection, animals were coregistered and mean images were created for a MCAo only, a vehicle (PBS) injection, as well as an ECM injection condition (Figure 7). In the MCAO only condition, no change of the CEST signal in the stroke area

was evident. A vehicle injection revealed a slight increase in the CEST signal in damaged tissue 1 day post-injection, but upon further inspection this was only evident in 1 animal out of 4. While the averaged $MTR_{asym}$ spectra showed little change at day 1 after the PBS injection (yellow vs. red, Fig. 7B), at day 3 and 7 the spectra became much lower. At 1.8 ppm, the $MTR_{asym}$ is 11.1%, 11.3%, 7.3%, and 6.4% for preinjection and day 1, 3, and 7 after PBS injection, respectively. Compared to the case without injection, the significant drop of $MTR_{asym}$ over time after the PBS injection indicated some physiological change caused by (or in response to) the injection, but the source is still unclear and requires further investigation. In contrast, in the ECM group a robust increase in the CEST signal was observed throughout the hyperintensity delineating the lesion cavity on the $T_2$-weighted MR image. The signal evident at 1 day post-implantation in ECM hydrogel implanted animals is hence selective to this material and reveals its in vivo distribution. However, by 3 days post-implantation the area of distribution was much reduced. By 7 days, no CEST signal above baseline could be detected. These visual representations are further supported by direct measurements of the $MTR_{asym}$ in the lesion area (Figure7B). A clear peak of the CEST signal is evident at 1.8 ppm with >20% $MTR_{asym}$ on day 1 after ECM injection. In contrast to the CEST image, at 7 days post-implantation there was still a robust histological evidence of ECM hydrogel present within ECM injected animals, whereas there was no material was present within MCAo only or PBS injected animals (Figure 7C). Nevertheless, there was evidence in 1 PBS animal that there was an upregulation of collagen I in a peri-infarct area, which

indicates an endogenous response to the injection of vehicle that is likely to upregulate ECM molecules to a level that is distinct from its pre-implantation state and sufficient to induce a small increase in CEST signal. However, this increase was evident in the other animals in this group indicating that an injection of a large volume of PBS inside damaged tissue, rather than the cavity, in this one animal might underlie these histological and imaging observations.

### 3.8. Time course comparison of CEST signal and ECM molecules in infarct and hydrogel

A comparison of the time course of the CEST signal with histology indicates that in MCAo only animals, the CEST signal is almost exclusively confined to the $T_2$-hyperintensity of the lesion corresponding histologically to the cavity, rather than surrounding damaged tissue, as indicated by GFAP reactivity of glia limitans (Figure 8A). Nevertheless, collagen I, chondroitin sulfate and fibronectin are all upregulated in this peri-infarct area compared to intact tissue. After ECM hydrogel injection, the cavity is filled with ECM hydrogel, as indicated by collagen I staining, corresponding to the area of increased CEST contrast. Still, some CEST signal is evident in damaged cortical regions, where no ECM hydrogel is evident. Chondroitin sulfate and fibronectin are also highly present within the ECM hydrogel hence providing a larger area of coverage, as well as a greater abundance of the molecules compared to the MCAo only condition (Figure 8B). By 7 days, the area and magnitude of the CEST signal is reduced, but the area covered by the ECM hydrogel still corresponds to the lesion cavity, hence

indicating a mismatch between the CEST signal and the ECM hydrogel due to the CEST signal returning to its baseline state. There is also a significant decrease in fibronectin within the ECM hydrogel and to a lesser degree a decrease in chondroitin sulfate that highlights the contribution of fibronectin and chondroitin sulfate to the specific and selective imaging of ECM after injection. The loss of these molecules is likely due to constructive remodelling, which eventually leads to a biodegradation of the ECM hydrogel.

## 4. Discussion

The use of extracellular matrix (ECM) as an inductive scaffolding material in regenerative medicine is finding wide-ranging applications [7], yet little advances have been achieved in monitoring the distribution and degradation of these bioscaffolds using non-invasive imaging [18]. Herein, we here demonstrate that ECM hydrogel has specific diamagnetic chemical exchange saturation transfer (diaCEST) properties that can be exploited to visualize its distribution acutely after implantation into a stroke cavity in the brain. Chondroitin sulfate and fibronectin are likely to be the main source of this effect, with the decrease of these molecules in the ECM hydrogel resulting in a return to the baseline CEST signal. Chondroitin sulfate and fibronectin within ECM hydrogel therefore provide specificity to the imaging approach, but their level of abundance conveys the selectivity to visualize the injected bioscaffold against the ECM background in the brain.

### 4.1. Specificity of ECM hydrogel detection by CEST imaging

The ECM is a collection of molecules that forms tissue out of cells [31]. Upon decellularization, these ECM molecules are retained and can be used for bioscaffolding [7, 32]. Non-invasive imaging of ECM molecules has mainly focussed on glycosaminoglycans (GAGs) due to their presence in intervertebrate discs and the clinical need to improve our ability to visualize its degradation. The assessment of GAG content can be achieved using CEST imaging [19, 33]. Implantation of a biomimetic ECM to promote cartilage regeneration indicated that these materials produce MRI characteristics similar to that of the native tissue [34, 35], but no gagCEST was performed to visualize the scaffold using its biochemical characteristics. Importantly four classes of GAGs can be recognized: heparin sulphate; chondroitin sulphate; keratin sulfate; and hyaluronic acid [36]. Indeed, chondroitin sulfate and hyaluronic acid are known to be present at a high concentration within the urinary bladder-derived ECM and detectable using immunohistochemistry against the lower abundance present within the native brain [8]. Our in vitro studies here showed that CS and HA induced CEST effects and potential for CEST imaging. Especially at 1.8 ppm, CS showed a marked effect with a 7% $MTR_{asym}$ effect compared to a 2.5% effect of HA. In contrast, collagen I which is highly present with ECM from urinary bladder exerted a negligible ~1% $MTR_{asym}$. Still, most ECM molecules tested here exhibited small effects between 0.2-2 ppm. Only CS and fibronectin exhibited wider chemical shifts. Indeed, chondroitin sulfate and fibronectin combined produce a $MTR_{asym}$

generally resembling the ECM profile, suggesting that the other molecules tested here exert a minor contribution to the CEST detection of ECM hydrogel. UBM-ECM-specific CEST imaging is hence feasible based on the $MTR_{asym}$ generated by CS and fibronectin. In contrast to ECM, the use of particular ECM molecules, such as HA, and its combination with other molecules potentially provides a mean to image those molecules more specifically in the absence of these in the native tissue [21]. However, a separation of individual molecules' signals will be challenging in a naturally mixed preparation, such as ECM, as there is a significant overlap between the $MTR_{asym}$ of these molecules.

The interaction and complexing of molecules in a mixed environment, such as the ECM, is also likely to influence the CEST effects that the individual molecules exert. Indeed, protein composition is known to affect biodegradation and rheological properties, which can affect MR parameters, such as T2 and diffusion [12, 37]. It was also evident here that detection of the CEST signal was influenced by the phase of the ECM (i.e. liquid versus cross-linked into a hydrogel). An overall decrease of the CEST signal was apparent. Importantly, at lower concentration with incomplete gelation [8], little distinction was, for instance, observed between 2 and 4 mg/mL in the hydrogel preparation. Still, a robust dose-dependence was evident indicating a linear relationship between concentrations >3 mg/mL and the CEST signal. Indeed, changes in the rheological properties due to cross-linking are likely to influence T2 signal, as well as NMR properties [38]. Although gagCEST is highly correlated with the T2 signal in native tissue [39], cross-linking of a hydrogel will not only influence

water content of the material leading to a decrease in T2 signal, but will also affect its NMR properties [40]. A transition here from the liquid phase to the hydrogel state resulted in an overall reduction of the $MTR_{asym}$. Still, an effect size of ~6% in vitro indicated potential for in situ visualization. Encouragingly, pH did not significantly affect the ECM hydrogel signal and the $MTR_{asym}$ was actually improved at physiological normothermia (i.e. 37 °C). A specific dose-dependent CEST signal of ECM hydrogel can hence be achieved that is marginally affected by pH and temperature.

### 4.2. Selective in vivo monitoring of hydrogel distribution and degradation

Injection of ECM hydrogel at 8 mg/mL afforded the detection of a specific CEST signal at 1.8 ppm that covered the lesion cavity. However, noise and background ECM signal required the application of a threshold to selectively visualize the signal increase. This signal was macroscopically corroborated by immunohistochemistry for the ECM hydrogel based on collagen I staining and was consistent with previous experiments [8]. However, a more detailed investigation of the correspondance between the CEST signal and the histological distribution of ECM hydrogel revealed small patches of mismatch, suggesting that damaged host tissue also produces a CEST signal at 1.8 ppm. Indeed, it is known that a variety of ECM molecules (e.g. chondroitin sulphate; fibronectin; laminin; collagen IV; hyaluronic acid) are upregulated in the peri-infarct area [41-44], as well as after intracerebral injection [45], thus compounding the “specific” CEST signal at 1.8 ppm. To distinguish this

endogenous upregulation of the CEST signal in the stroke brain from the ECM hydrogel injected signal, acquisition of a baseline pre-implantation image allowed us to subtract this endogenous baseline signal from the post-implant CEST to reveal changes due to the injected material. This produced a selective visualization of the ECM hydrogel distribution at day 1, but also indicated that an additional upregulation of endogenous ECM molecules can be caused by injection damage to the peri-infarct region. These results hence indicate that ECM hydrogel can be detected selectively, but that interpretation of any CEST changes needs to include a careful consideration of alternative endogenous sources of contrast.

Considering the microenvironment inside the lesion cavity, semi-solid macromolecular magnetization transfer (MT), as well as water proton saturation (spillover), provide competing signals influencing CEST imaging within a stroke lesion [46, 47]. Nevertheless, the magnitude of increase in $MTR_{asym}$ due to the ECM injection against the stroke environment is ~10% providing a robust detection of distribution within the lesion, but also erroneous hydrogel localization, for instance in the ventricle. This demonstrates the usefulness of this approach to map the delivery and initial distribution of the ECM hydrogel within the stroke lesion environment, akin to our previous report using immunohistochemical methods to detect ECM hydrogel [8]. Still, the degradation of the material reduced the abundance of ECM molecules and within 3 days mostly returned to baseline. Remodeling of the ECM lead to a decrease in fibronectin and chondroitin sulphate, which is likely to account for the decrease in

CEST signal. However, ECM material here resulted in a fairly broad CEST effect with specific peaks at 1.8 and 3.6 ppm, which is more weighted by chondroitin sulfate and fibronectin. While the 3.6 ppm signal is likely due to the amide-water proton transfer effects [25], the exact source of the 1.8 ppm signal is not clear. The signal reaches maximum with a relatively high power of 220Hz, suggesting a fast chemical exchange rate. Thus, it may arise from hydroxyl protons, which have a chemical shift of 1-3 ppm from water [48], or amine groups from the side chain of mobile proteins [49, 50]. Interestingly, others reported similar CEST effects (also at 1.8 and 3.6 ppm) using hyaluronic acid hydrogels supplemented with gelatin [21]. In order to quantify the degradation of the biomaterial more accurately, implementation of imaging approaches geared towards measuring the macromolecular tissue volume might be needed [51], whereas monitoring the degradation of specific ECM molecules would require their tethering to contrast agents, such as gadolinium [14].

## 5. Conclusions

dia-CEST imaging is an exciting new imaging technique to non-invasively visualize hydrogels of different constituents. Herein, we demonstrated that it affords the selective visualization of an ECM hydrogel injected into a stroke-cavity by targeting a specific frequency at which the “contrast” is tuned towards chondroitin sulfate and fibronectin. Although the imaging is robust towards changes in pH and temperature, other molecules can exert similar effects as the CEST signal is not directly detecting ECM molecules, but is sensitive towards

their labile proton content, and both hydroxyl and amine signals may contribute in this frequency range. A further consideration is that endogenous ECM also exert a minor CEST effect which is upregulated in the area of infarction, hence requiring subtraction of a baseline CEST imaging to provide a truly selective imaging of the distribution of ECM hydrogel distribution. Certainly, specific and selective monitoring of the ECM hydrogel and its degradation requires further development of the imaging approach, but also advances in tuning material properties that can improve their detection against host background.

**Acknowledgements**

This study was funded by a seed grant from the Department of Health of the Commonwealth of Pennsylvania (4100068505) and the National Institute for Neurological Disease and Stroke (R01NS08226). The authors thank Dr Wen Ling for acquiring pilot data, Ms Madeline Gerwig for sectioning the brains, and Brendon Wahlberg for post-op care of MCAO animals.

**Author Contributions**

JT set-up, acquired and developed the post-processing of dia-CEST images. FJN prepared all samples, performed MCAo surgery and ECM implantation and perfused animals. WC performed co-registration, group mapping and statistical image comparisons. HG performed immunohistochemistry and acquired histology images. SFB provided the ECM hydrogel. MM conceived of the study,

provided funding, oversaw the acquisition and analysis and also drafted the manuscript. All authors read and approved the manuscript.

## References


[1] Nicholson C, Sykova E. Extracellular space structure revealed by diffusion analysis. Trends Neurosci. 1998;21:207-15.

[2] Ashioti M, Beech JS, Lowe AS, Hesselink MB, Modo M, Williams SC. Multi-modal characterisation of the neocortical clip model of focal cerebral ischaemia by MRI, behaviour and immunohistochemistry. Brain Res. 2007;1145:177-89.

[3] Smith EJ, Stroemer RP, Gorenkova N, Nakajima M, Crum WR, Tang E, et al. Implantation site and lesion topology determine efficacy of a human neural stem cell line in a rat model of chronic stroke. Stem Cells. 2012;30:785-96.

[4] Bible E, Chau DY, Alexander MR, Price J, Shakesheff KM, Modo M. The support of neural stem cells transplanted into stroke-induced brain cavities by PLGA particles. Biomaterials. 2009;30:2985-94.

[5] Park KI, Teng YD, Snyder EY. The injured brain interacts reciprocally with neural stem cells supported by scaffolds to reconstitute lost tissue. Nat Biotechnol. 2002;20:1111-7.

[6] Bible E, Dell'Acqua F, Solanky B, Balducci A, Crapo PM, Badylak SF, et al. Non-invasive imaging of transplanted human neural stem cells and ECM scaffold remodeling in the stroke-damaged rat brain by (19)F- and diffusion-MRI. Biomaterials. 2012;33:2858-71.

[7] Brown BN, Badylak SF. Extracellular matrix as an inductive scaffold for functional tissue reconstruction. Transl Res. 2014;163:268-85.

[8] Massensini AR, Ghuman H, Saldin LT, Medberry CJ, Keane TJ, Nicholls FJ, et al. Concentration-dependent rheological properties of ECM hydrogel for intracerebral delivery to a stroke cavity. Acta Biomater. 2015;27:116-30.

[9] Bible E, Chau DY, Alexander MR, Price J, Shakesheff KM, Modo M. Attachment of stem cells to scaffold particles for intra-cerebral transplantation. Nat Protoc. 2009;4:1440-53.

[10] Wang AM, Cao P, Yee A, Chan D, Wu EX. Detection of extracellular matrix degradation in intervertebral disc degeneration by diffusion magnetic resonance spectroscopy. Magn Reson Med. 2015;73:1703-12.

[11] Cheng HL, Islam SS, Loai Y, Antoon R, Beaumont M, Farhat WA. Quantitative magnetic resonance imaging assessment of matrix development in cell-seeded natural urinary bladder smooth muscle tissue-engineered constructs. Tissue Eng Part C Methods. 2010;16:643-51.

[12] Cheng HL, Loai Y, Farhat WA. Monitoring tissue development in acellular matrix-based regeneration for bladder tissue engineering: multiexponential diffusion and T2* for improved specificity. NMR Biomed. 2012;25:418-26.

[13] Hu J, Liu C, Chen L, Xing W, Luan J. Volumetric measurement of polyacrylamide hydrogel injected for breast augmentation using magnetic resonance imaging. Exp Ther Med. 2014;7:681-4.

[14] Berdichevski A, Shachaf Y, Wechsler R, Seliktar D. Protein composition alters in vivo resorption of PEG-based hydrogels as monitored by contrast-enhanced MRI. Biomaterials. 2015;42:1-10.

[15] Yang X, Sun Y, Kootala S, Hilborn J, Heerschap A, Ossipov D. Injectable hyaluronic acid hydrogel for 19F magnetic resonance imaging. Carbohydr Polym. 2014;110:95-9.

[16] Zhang Y, Sun Y, Yang X, Hilborn J, Heerschap A, Ossipov DA. Injectable in situ forming hybrid iron oxide-hyaluronic acid hydrogel for magnetic resonance imaging and drug delivery. Macromol Biosci. 2014;14:1249-59.

[17] Modo M, Kolosnjaj-Tabi J, Nicholls F, Ling W, Wilhelm C, Debarge O, et al. Considerations for the clinical use of contrast agents for cellular MRI in regenerative medicine. Contrast Media Mol Imaging. 2013;8:439-55.

[18] Naumova AV, Modo M, Moore A, Murry CE, Frank JA. Clinical imaging in regenerative medicine. Nat Biotechnol. 2014;32:804-18.

[19] Ling W, Regatte RR, Navon G, Jerschow A. Assessment of glycosaminoglycan concentration in vivo by chemical exchange-dependent saturation transfer (gagCEST). Proc Natl Acad Sci U S A. 2008;105:2266-70.

[20] Saar G, Zhang B, Ling W, Regatte RR, Navon G, Jerschow A. Assessment of glycosaminoglycan concentration changes in the intervertebral disc via chemical exchange saturation transfer. NMR Biomed. 2012;25:255-61.
[21] Liang Y, Bar-Shir A, Song X, Gilad AA, Walczak P, Bulte JW. Label-free imaging of gelatin-containing hydrogel scaffolds. Biomaterials. 2015;42:144-50.
[22] Kim M, Gillen J, Landman BA, Zhou J, van Zijl PC. Water saturation shift referencing (WASSR) for chemical exchange saturation transfer (CEST) experiments. Magn Reson Med. 2009;61:1441-50.
[23] Jin T, Autio J, Obata T, Kim SG. Spin-locking versus chemical exchange saturation transfer MRI for investigating chemical exchange process between water and labile metabolite protons. Magn Reson Med. 2011;65:1448-60.
[24] Jin T, Kim SG. Advantages of chemical exchange-sensitive spin-lock (CESL) over chemical exchange saturation transfer (CEST) for hydroxyl- and amine-water proton exchange studies. NMR Biomed. 2014;27:1313-24.
[25] Zhou J, Payen JF, Wilson DA, Traystman RJ, van Zijl PC. Using the amide proton signals of intracellular proteins and peptides to detect pH effects in MRI. Nat Med. 2003;9:1085-90.
[26] Modo M, Stroemer RP, Tang E, Veizovic T, Sowniski P, Hodges H. Neurological sequelae and long-term behavioural assessment of rats with transient middle cerebral artery occlusion. J Neurosci Methods. 2000;104:99-109.
[27] Modo M. Long-term survival and serial assessment of stroke damage and recovery - practical and methodological considerations. J Exp Stroke Transl Med. 2009;2:52-68.
[28] Stille M, Smith EJ, Crum WR, Modo M. 3D reconstruction of 2D fluorescence histology images and registration with in vivo MR images: application in a rodent stroke model. J Neurosci Methods. 2013;219:27-40.
[29] Crum WR, Modo M, Vernon AC, Barker GJ, Williams SC. Registration of challenging pre-clinical brain images. J Neurosci Methods. 2013;216:62-77.
[30] Jenkinson M, Bannister P, Brady M, Smith S. Improved optimization for the robust and accurate linear registration and motion correction of brain images. Neuroimage. 2002;17:825-41.
[31] Zimmermann DR, Dours-Zimmermann MT. Extracellular matrix of the central nervous system: from neglect to challenge. Histochem Cell Biol. 2008;130:635-53.
[32] Meng F, Modo M, Badylak SF. Biologic scaffold for CNS repair. Regen Med. 2014;9:367-83.
[33] Schleich C, Muller-Lutz A, Zimmermann L, Boos J, Schmitt B, Wittsack HJ, et al. Biochemical imaging of cervical intervertebral discs with glycosaminoglycan chemical exchange saturation transfer magnetic resonance imaging: feasibility and initial results. Skeletal Radiol. 2016;45:79-85.
[34] Ravindran S, Kotecha M, Huang CC, Ye A, Pothirajan P, Yin Z, et al. Biological and MRI characterization of biomimetic ECM scaffolds for cartilage tissue regeneration. Biomaterials. 2015;71:58-70.
[35] Kotecha M, Klatt D, Magin RL. Monitoring cartilage tissue engineering using magnetic resonance spectroscopy, imaging, and elastography. Tissue Eng Part B Rev. 2013;19:470-84.
[36] Sasisekharan R, Raman R, Prabhakar V. Glycomics approach to structure-function relationships of glycosaminoglycans. Annu Rev Biomed Eng. 2006;8:181-231.
[37] Cheng HL, Loai Y, Beaumont M, Farhat WA. The acellular matrix (ACM) for bladder tissue engineering: A quantitative magnetic resonance imaging study. Magn Reson Med. 2010;64:341-8.
[38] Nigmatullin R, Bencsik M, Gao F. Influence of polymerisation conditions on the properties of polymer/clay nanocomposite hydrogels. Soft Matter. 2014;10:2035-46.
[39] Muller-Lutz A, Schleich C, Schmitt B, Antoch G, Matuschke F, Quentin M, et al. Gender, BMI and T2 dependencies of glycosaminoglycan chemical exchange saturation transfer in intervertebral discs. Magn Reson Imaging. 2015.
[40] Onuki Y, Hasegawa N, Kida C, Obata Y, Takayama K. Study of the contribution of the state of water to the gel properties of a photocrosslinked polyacrylic acid hydrogel using magnetic resonance imaging. J Pharm Sci. 2014;103:3532-41.

[41] Ji K, Tsirka SE. Inflammation modulates expression of laminin in the central nervous system following ischemic injury. J Neuroinflammation. 2012;9:159.
[42] Al'Qteishat A, Gaffney J, Krupinski J, Rubio F, West D, Kumar S, et al. Changes in hyaluronan production and metabolism following ischaemic stroke in man. Brain. 2006;129:2158-76.
[43] Li L, Liu F, Welser-Alves JV, McCullough LD, Milner R. Upregulation of fibronectin and the alpha5beta1 and alphavbeta3 integrins on blood vessels within the cerebral ischemic penumbra. Exp Neurol. 2012;233:283-91.
[44] Huang L, Wu ZB, Zhuge Q, Zheng W, Shao B, Wang B, et al. Glial scar formation occurs in the human brain after ischemic stroke. Int J Med Sci. 2014;11:344-8.
[45] Gates MA, Laywell ED, Fillmore H, Steindler DA. Astrocytes and extracellular matrix following intracerebral transplantation of embryonic ventral mesencephalon or lateral ganglionic eminence. Neuroscience. 1996;74:579-97.
[46] Zaiss M, Xu J, Goerke S, Khan IS, Singer RJ, Gore JC, et al. Inverse Z-spectrum analysis for spillover-, MT-, and T1 -corrected steady-state pulsed CEST-MRI--application to pH-weighted MRI of acute stroke. NMR Biomed. 2014;27:240-52.
[47] Li H, Zu Z, Zaiss M, Khan IS, Singer RJ, Gochberg DF, et al. Imaging of amide proton transfer and nuclear Overhauser enhancement in ischemic stroke with corrections for competing effects. NMR Biomed. 2015;28:200-9.
[48] van Zijl PC, Jones CK, Ren J, Malloy CR, Sherry AD. MRI detection of glycogen in vivo by using chemical exchange saturation transfer imaging (glycoCEST). Proc Natl Acad Sci U S A. 2007;104:4359-64.
[49] Desmond KL, Moosvi F, Stanisz GJ. Mapping of amide, amine, and aliphatic peaks in the CEST spectra of murine xenografts at 7 T. Magn Reson Med. 2014;71:1841-53.
[50] Jin T, Wang P, Zong X, Kim SG. Magnetic resonance imaging of the Amine-Proton EXchange (APEX) dependent contrast. Neuroimage. 2012;59:1218-27.
[51] Mezer A, Yeatman JD, Stikov N, Kay KN, Cho NJ, Dougherty RF, et al. Quantifying the local tissue volume and composition in individual brains with magnetic resonance imaging. Nat Med. 2013;19:1667-72.

## Figure Legends

**Figure 1. Characterizing the CEST effect of ECM hydrogel. A**. In vitro z spectra of 8 mg/mL ECM hydrogel at different frequencies allowed us to assay if there are any chemical exchange sites that affect the magnetization transfer from the saturation signal ($S_{Sat}$) and could be exploited for a direct imaging approach. **B.** To more clearly visualize the exchange sites, the magnetization transfer asymmetry ($MTR_{asym}$) was plotted to reveal distinct exchange sites at frequencies <750 Hz. The most pronounced effect in these sites was observed at 220 Hz, which was used for all subsequent imaging. **C**. CEST images at these frequencies for different exchange sites further illustrate the potential of this approach to afford a visualization of ECM hydrogel.

**Figure 2. Influence of experimental conditions on CEST signal.** To evaluate how temperature and pH affect the detection of a specific signal from the 8 mg/mL hydrogel upon implantation into the brain, temperature (21 °C, 30 °C, 37 °C) and pH (5.5, 6.0, 6.5, 7.0) were arrayed with the acquisition of a full z spectra and displayed as $MTR_{asym}$ plots **(A)**. Detection of ECM can be further affected by its concentration (2, 4, 6, 8 mg/mL), as well as its state being in liquid form **(B)** or cross-linked as a hydrogel **(C)**. A 0 mg/mL condition, consisting of PBS only, served as a control. Pepsin is also added to the ECM preparation in a concentration-dependent fashion and could hence be a confounding factor, but no effect of pepsin on the CEST signal was found here at any concentration **(D)**.

**Figure 3. Detection of individual ECM components. A.** $MTR_{asym}$ plots of individual ECM molecules found in ECM hydrogel. Specifically, Chondroitin Sulfate (CS), vitronectin (Vitro), collagen I (Coll I) and IV (Coll IV), fibronectin (Fib), Heparin Sulfate (Hep), hyaluronic acid (HA) and laminin (Lam) were evaluated as potential candidates for the signal detected in the ECM hydrogel preparation. As a potential confound in vivo, artificial cerebrospinal fluid (aCSF) was also assayed for its $MTR_{asym}$. **B.** As CS and Fib exhibited individual $MTR_{asym}$ signal that resemble the ECM hydrogel when combined, both were combined into a single preparation to determine if these are the dominant source of the $MTR_{asym}$ in the ECM hydrogel.

**Figure 4. Acute in vivo detection of ECM hydrogel implanted in a stroke cavity. A.** CEST imaging of 8 mg/mL ECM hydrogel 24 hours after injection into the stroke cavity in 3 different animals revealed a signal that corresponded to the expected coverage of the lesion cavity. **B.** Anterior-posterior slices further highlight the coverage of the entire lesion cavity and its validation by histological analysis (ECM hydrogel detected by collagen I staining). **C.** A more detailed examination of the correspondence between the CEST and histological detection of the ECM hydrogel reveal a good overlap (blue arrows), but also point out some discrepancies. In some cases, the CEST signal corresponded to the $T_2$-weighted lesion environment, but there was no evidence of ECM hydrogel present in this area (*). In other instances, a mismatch indicated a CEST signal in an area with damaged host tissue (*), but no significant ECM hydrogel being

present. **D.** Still, ECM hydrogel leaking into the lateral ventricle due to injection tract damage can be selectively visualized using this approach indicating its validity to assay the macroscopic distribution of ECM hydrogel injections.

**Figure 5. Stroke microenvironment-specific CEST signals and specificity of ECM hydrogel signal**. A comparison of the CEST signal within the lesion cavity, homologous contralateral tissue, as well as the lateral ventricle reveal a weak (<5%) endogenous CEST signal at 1.8 ppm, which is upregulated in the lesion cavity (~8%). However, injection of ECM hydrogel within this same environment lead to an increase of the signal to >20% by 1 day post-implantation.

**Figure 6. Serial in vivo detection of ECM hydrogel implanted in a stroke cavity.** To probe the utility of this imaging approach in monitoring the presence and potential biodegradation of the ECM hydrogel over time, serial MR imaging was performed prior to the injection of the ECM hydrogel (Pre), as well as 1, 3 and 7 days post-implantation. To account for a baseline CEST signal, the pre-implant images were subtracted from post-implant time points with thresholding of ±3 standard deviations (sd) being applied to filter out noise. $MTR_{asym}$ plots show the evolution of the signal inside the lesion cavity for individual animals. Histological analyses further corroborated the detection and distribution of ECM hydrogel based on collagen I staining, as well as the delineation of the lesion cavity based on glial scarring as indicated by GFAP staining.

**Figure 7. Group comparison of CEST signal. A**. To afford a group comparison, individual animals were co-registered and images were average to provide a representative mean group image for each time point. In MCAo only animals, no CEST signal was evident at any time point when accounting for the baseline signal and thresholding. For PBS (i.e. vehicle) injected animals, an acute signal change was observed. This was due to 1 animal having an elevated CEST signal on 1 day, potentially reflecting an increase in host chondroitin sulfate and fibronectin due to injection damage. However, a clear increase in CEST signal was evident in the ECM injected group at 1 day post-injection, but this signal gradually decrease by 3 days and no longer warranted detection at 7 days. **B.** Group $MTR_{asym}$ plots for signal inside the lesion cavity further supported the changes observed on the mean images. **C.** A representative histology image further corroborated the lack of ECM material in the lesion cavity in MCAo only and PBS animals, but a robust coverage in ECM hydrogel injected animals (*). In a PBS injected animal, an upregulation of collagen I (Coll I) was observed in the peri-infarct area (red arrow), but this was not evident in the MCAo only animals. In ECM hydrogel injected animals, there was also evidence of an upregulation of collagen I staining in the peri-infarct area including the lesioned cortex (blue arrow). However the degree of increase was markedly higher than in PBS animals and is likely to reflect some of the ECM hydrogel having permeated into this area during the injection procedure.

**Figure 8. Histological validation of in vivo imaging. A**. A direct comparison between the lesion environment and the CEST signal indicates that a strong signal (thresholded to 3 standard deviations of the contralateral hemisphere) can be detected in the stroke area in MCAo animals. The CEST signal detected here is hence not by itself specific to the ECM hydrogel, but is based on the CEST effect of ECM molecules that are also upregulated after a stroke. Indeed, collagen I (Coll I), chondroitin sulfate (CS) and fibronectin (Fib) are found to be significantly upregulated in the lesion area compared to the contralateral hemisphere and hence provide a biological source for this increase CEST signal. Nevertheless, the injection of an ECM hydrogel further enhances this endogenous signal, specifically in the area where ECM hydrogel was injected into the lesion cavity with chondroitin sulfate and fibronectin being strongly present within the injected material at 1 day, but less so at 7 days. At 7 days post-injection, this signal is reduced to baseline. Especially fibronectin appears reduced at 7 days within the ECM hydrogel, with chondroitin sulfate showing a less marked decrease and collagen I showing little difference to the 1 day time point. **B.** Overlay images for 1 and 7 days post-injection further highlight the differences in chondroitin sulfate and fibronectin (adjacent sections) in the ECM hydrogel (collagen I), as well as at the interface with damaged host tissue. Fibronectin and chondroitin sulphate are highly present within the ECM on day 1 post-injection (i), but appear to be reduced by 7 days post-injection (ii).

## Tables

| Component | Concentration (mg/mL) | Company | Catalogue # |
|---|---|---|---|
| Chondroitin Sulfate | 3 | Sigma | C9819 |
| Collagen I | 3 | BD | 354236 |
| Collagen IV | 1 | Sigma | C7521 |
| Fibronectin | 1 | Sigma | F1141 |
| Heparin Sulfate | 1 | Sigma | H7640 |
| Hyaluronic Acid | 5 | Sigma | 53747 |
| Laminin | 1 | Sigma | L2020 |
| Vitronectin | 0.8 | Sigma | SRP3186 |

**Table 1. List of individual ECM components.**

## Supplementary Figures

**Supplementary Figure 1. $MTR_{asym}$ thresholding and signal evolution over time**. To highlight the $MTR_{asym}$ above and below what can be considered noise and the standard endogenous signal, the mean $MTR_{asym}$ of the contralateral hemisphere was measured, including its standard deviation (sd), and a threshold of 3 sd was applied to yield a representation of the signal that was significantly above the baseline of non-damaged brain tissue. This thresholding afforded a visualization of the evolution of changes over time in MCAo only, as well as ECM implanted animals. It is evident here that there is a significant increase in $MTR_{asym}$ in the MCAo only control condition that needs to be subtracted to afford a visualization of the ECM hydrogel's contribution to the $MTR_{asym}$.

**Supplementary Figure 2. Baseline CEST signal subtraction and thresholding**. To account for the baseline signal present within the stroke lesion, as well as the non-damaged brain, CEST images from the pre-implant time point were subtracted (Sub.) from post-implant time points. To eliminate noise from these images, a threshold was applied. In the MCAo only animals, it is evident 3 standard deviations (sd) provide a sufficient threshold to eliminate noise from these images. Upon application of this approach to ECM hydrogel implanted animals, this afforded the selective visualization of the injected material to the CEST signal detected within the lesion cavity.

**Supplementary Figure 3. Matristem detection**. To ensure that our detection here is not specific to our preparation of ECM hydrogel, the equivalent commercially available preparation Matristem was also evaluated. Matristem yielded an equivalent detection **(A)** compared to the concentration used here **(B),** but provided a better distinction between different concentrations and produced a more robust effect.

**Figure 1**

Click here to download high resolution image

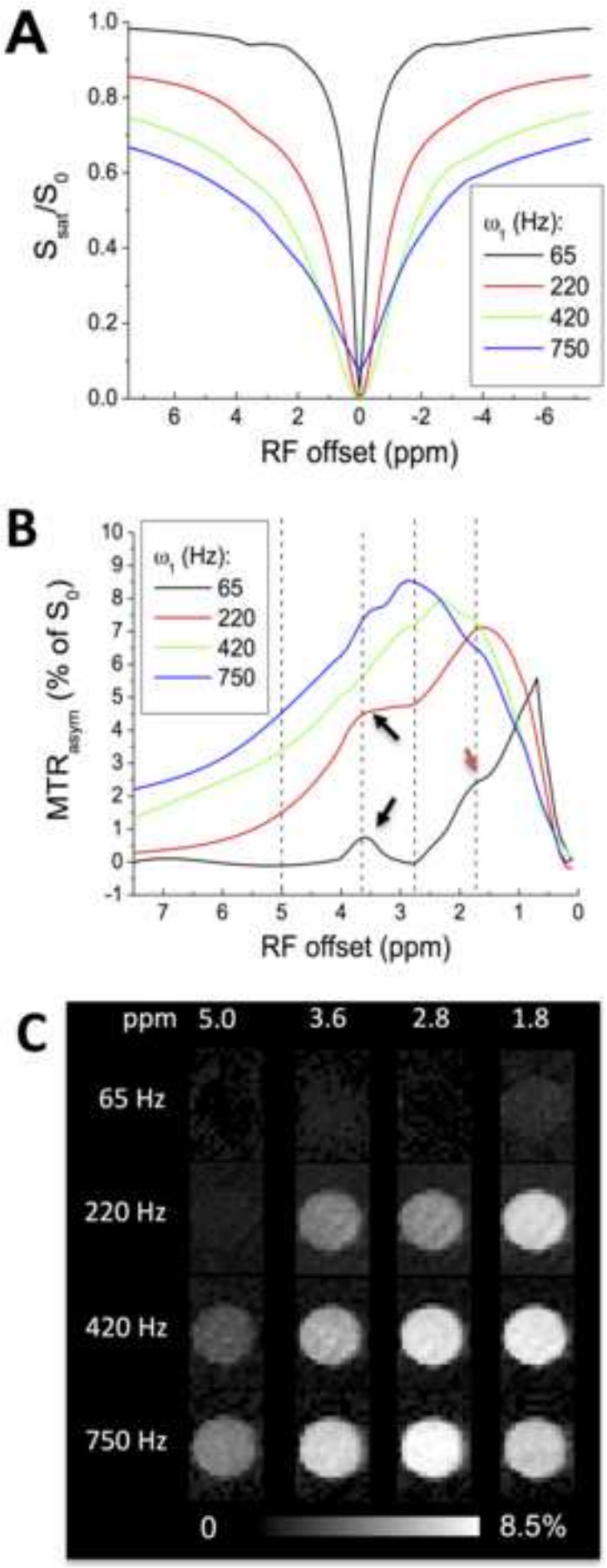

Figure 2

Click here to download high resolution image

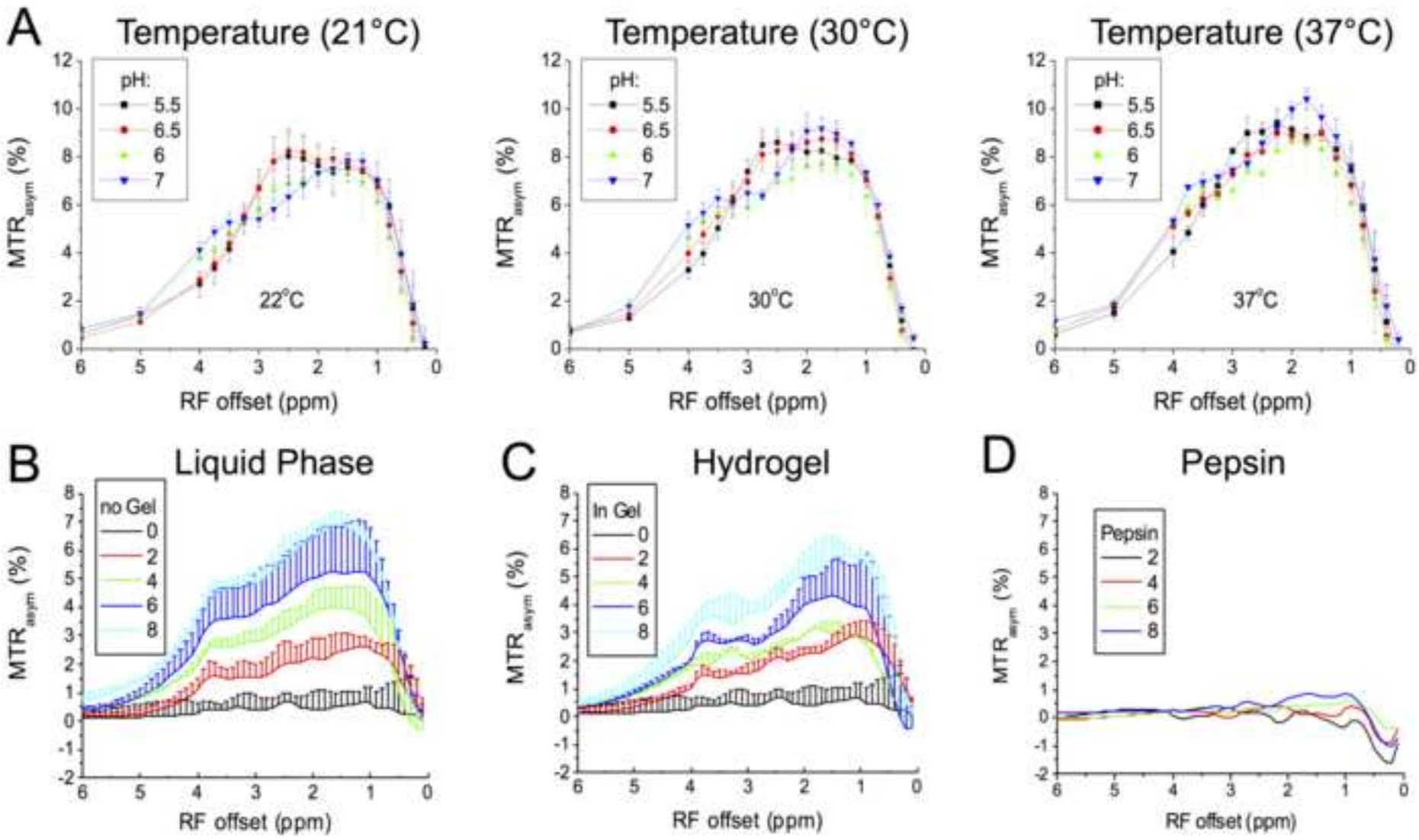

Figure 3

Click here to download high resolution image

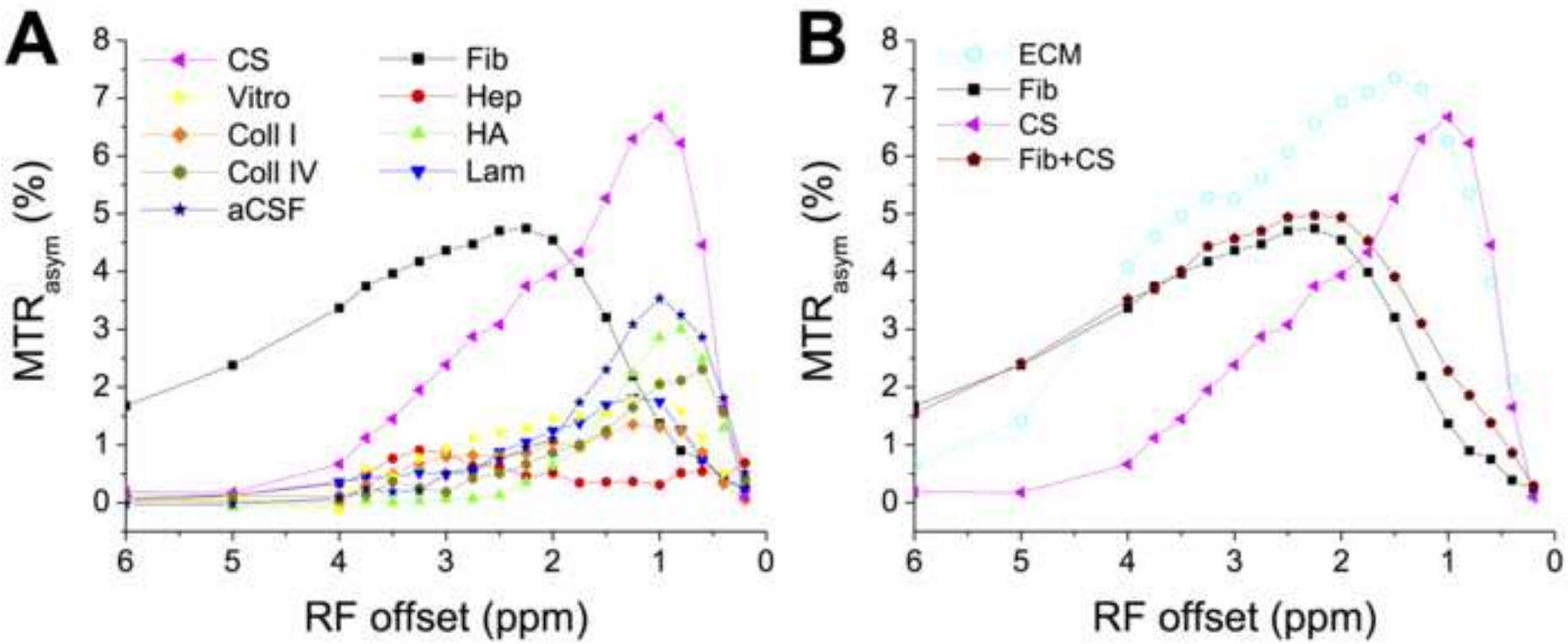

**Figure 4**

Click here to download high resolution image

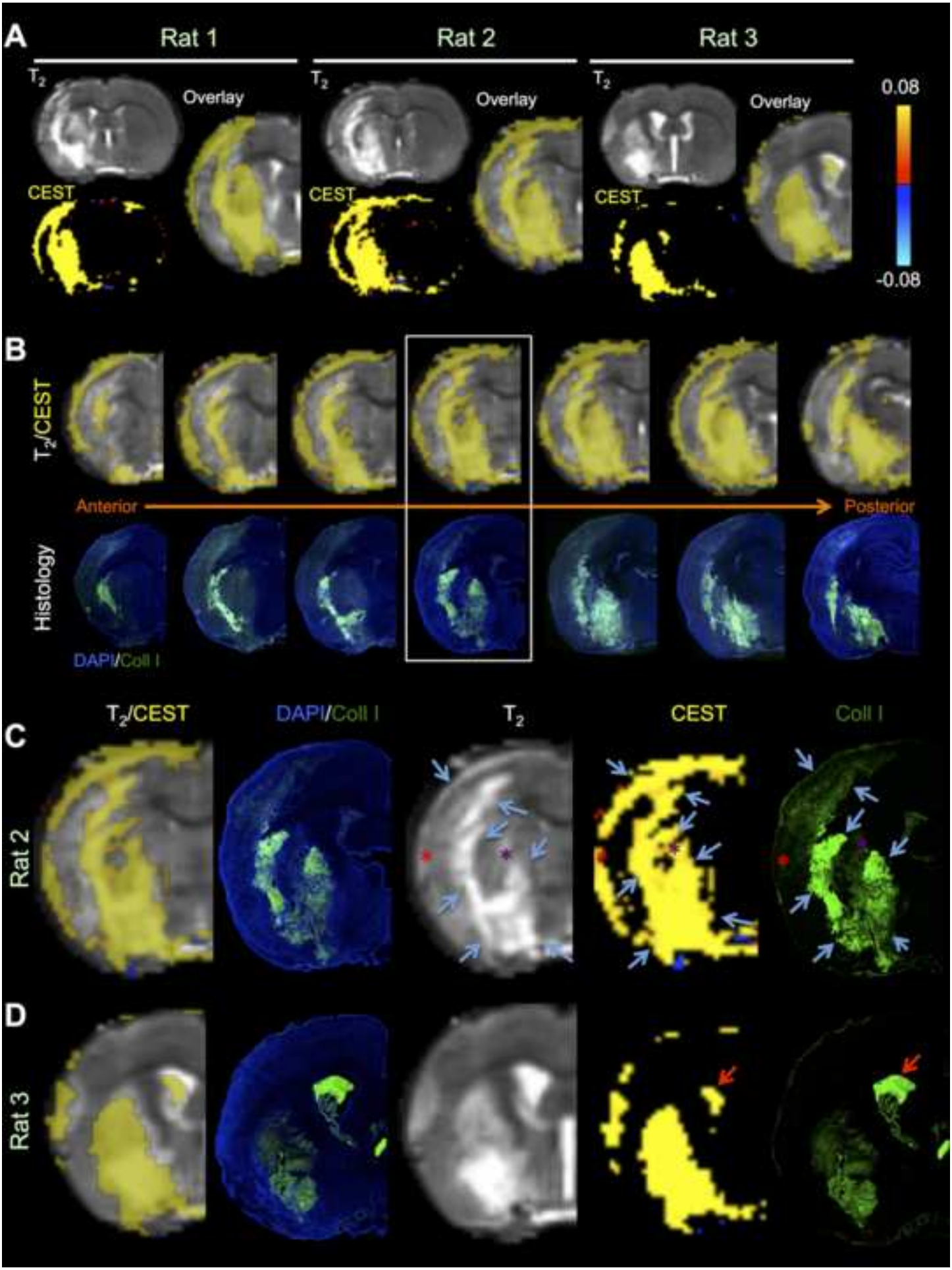

**Figure 5**

Click here to download high resolution image

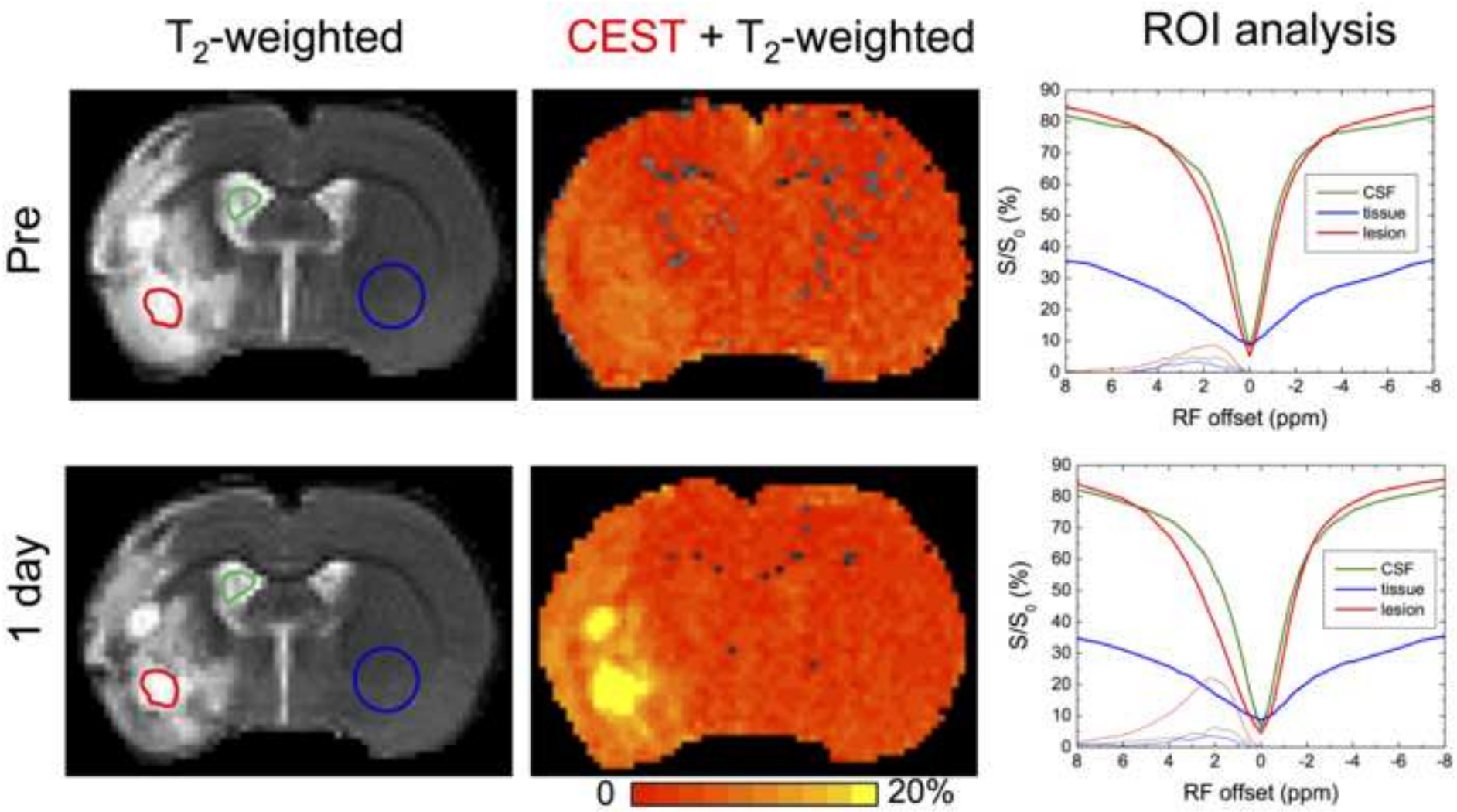

**Figure 6**

**Click here to download high resolution image**

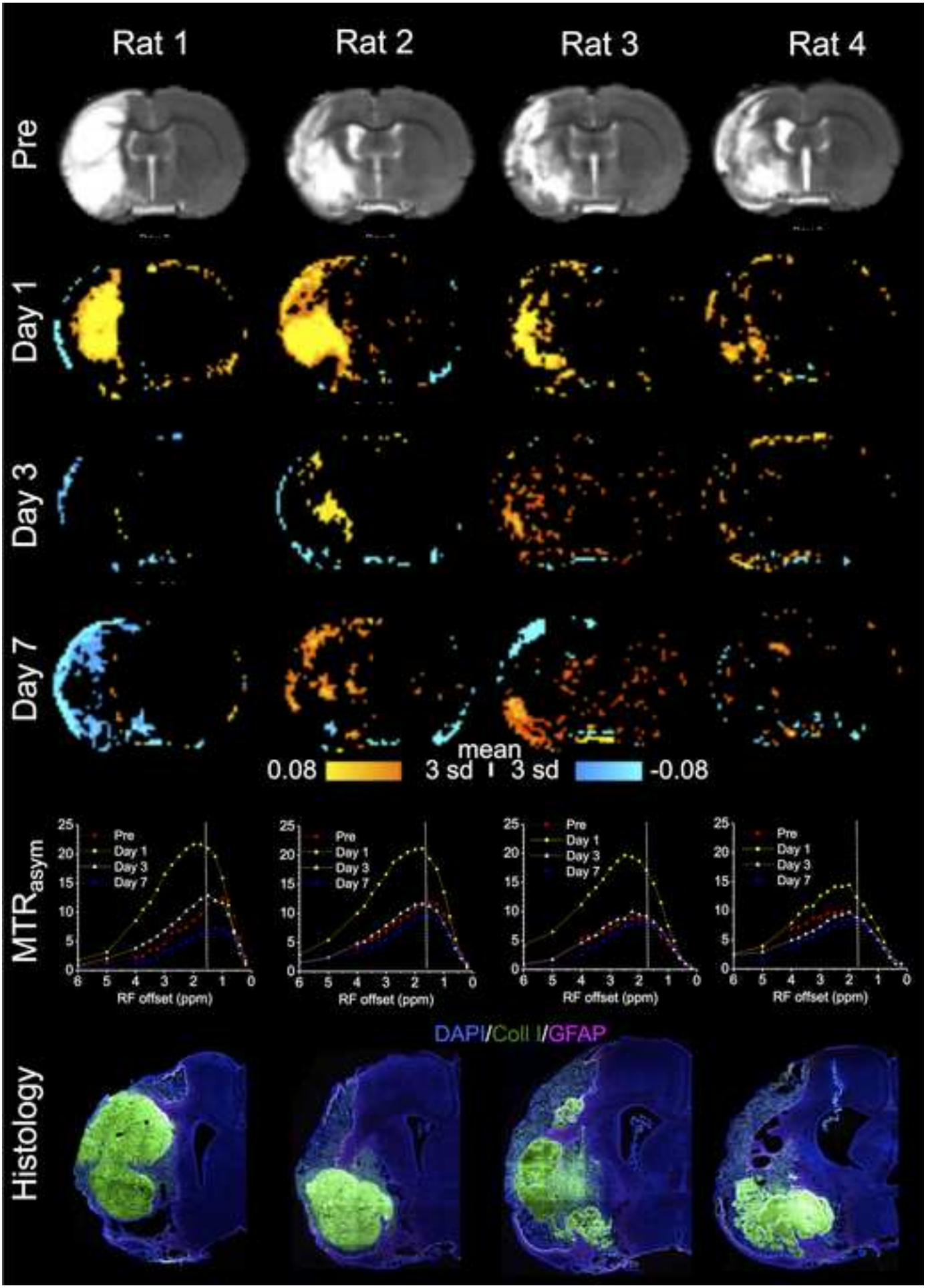

**Figure 7**

**Click here to download high resolution image**

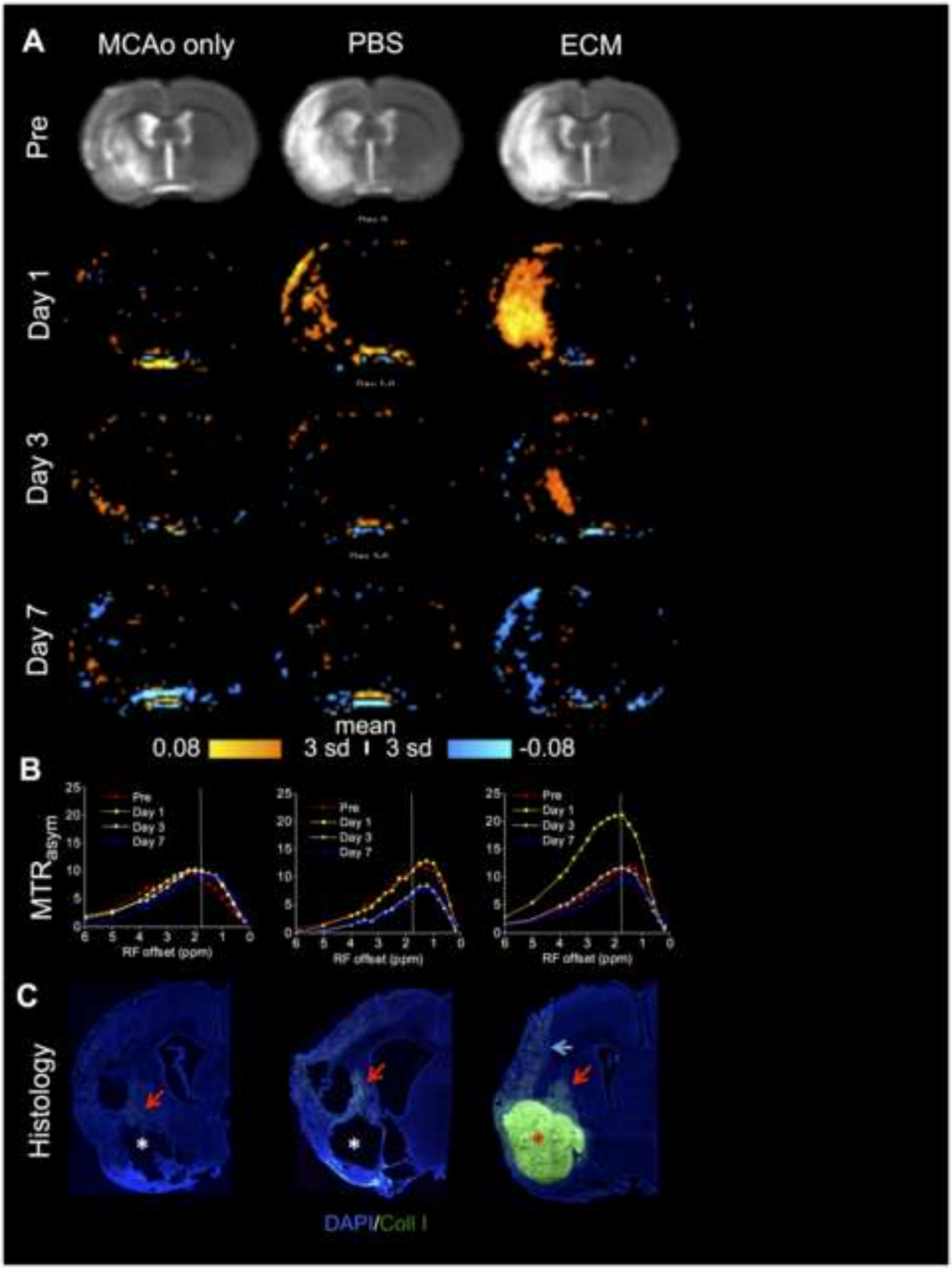

**Figure 8**

Click here to download high resolution image